

# Modelling the thermosolutal convection, shrinkage flow and grain movement of globular equiaxed solidification using a three phase model

T. Wang<sup>\*1,3</sup>, M. Wu<sup>2</sup>, A. Ludwig<sup>2</sup>, M. Abondano<sup>1</sup>, B. Pustal<sup>1</sup> and A. Bührig-Polaczek<sup>1</sup>

<sup>1</sup>Foundry Institute, Aachen University of Technology, Intzestr.5, Aachen, D-52072, Germany

<sup>2</sup>Department of Metallurgy, University of Leoben, Franz-Josef-Str.18, Leoben, A-8700, Austria

<sup>3</sup>Department of Material, Dalian University of Technology, Linggong road 2, 116024, China

A three phase volume averaging model has been developed to simulate globular equiaxed solidification, the three phases being liquid, solid and air. The basic conservation equations of mass, momentum and enthalpy have been solved for each phase, and the thermal and mechanical (drag force) interactions among the phases have been considered. Grain nucleation, growth rate (mass exchange), solute partitioning at the liquid/solid interface and solute transport have also been accounted for. Due to its low density, the air phase floats always at the top region, forming a definable air/liquid melt interface, i.e. free surface. By tracking this free surface, the shrinkage cavity in an open casting system can be modelled. As the temperature and concentration dependent density and solidification shrinkage are explicitly included, the thermosolutal convection, together with feeding flow and grain movement can be taken into account. This paper focuses on the model description; preliminary results on a benchmark ingot casting (Al-4Cu) are presented and discussed. **IJC/545**

© 2005 W. S. Maney & Son Ltd. Manuscript received 22 September 2004; accepted 6 January 2005.

**Keywords:** Three phase; Free surface; Thermosolutal convection; Shrinkage flow; Grain movement

## List of symbols

$C^*$	species concentration in interface
$c_l, c_s$	species mass concentration
$c_p(l), c_p(s), c_p(a)$	specific heat, $\text{J kg}^{-1} \text{K}^{-1}$
$C_D$	drag coefficient
$C_{ls}(= -C_{sl})$	species exchange rate, $\text{kg m}^{-3} \text{s}^{-1}$
$C_{ls}^P$	species exchange due to phase change, $\text{kg m}^{-3} \text{s}^{-1}$
$C_p(\phi_c)$	dendrite shape factor
$d_a$	particle size of air, m
$d_s$	grain diameter, m
$D_l, D_s$	solute diffusion coefficient, $\text{m}^2 \text{s}^{-1}$
$f_l, f_s, f_a$	volume fraction
$f_s^c$	grain packing limit

$g$	gravity acceleration, $\text{m s}^{-2}$
$g_z$	growth factor, $\text{m s}^{-1}$
$h_l, h_s, h_a$	enthalpy, $\text{J kg}^{-1}$
$H_{la}, H_{sa}$	heat transfer coefficient, $\text{W m}^{-2} \text{K}^{-1}$
$k$	partition coefficient of phase diagram
$k_l, k_s, k_a$	thermal conductivity, $\text{W m}^{-1} \text{K}^{-1}$
$K_{ls}, k_{la}, k_{sa}$	momentum exchange coefficient, $\text{kg m}^{-3} \text{s}^{-1}$
$m$	slope of liquidus in phase diagram, K
$M_{ls}(= -M_{sl})$	mass transfer rate, $\text{kg s}^{-1} \text{m}^{-3}$
$n$	grain density, $\text{m}^{-3}$
$n_{\max}$	maximum grain density, $\text{m}^{-3}$
$N$	grain production rate, $\text{m}^{-3} \text{s}^{-1}$
$Nu_p$	Nusselt number
$p$	pressure, Pa
$Q_{ls}(= -Q_{ls}),$ $Q_{la}(= -Q_{al}),$ $Q_{sa}(= -Q_{as})$	energy exchange rate, $\text{J m}^{-3} \text{s}^{-1}$
$Q_{la}^d, Q_{sa}^d$	energy exchange by heat transfer, $\text{J m}^{-3} \text{s}^{-1}$
$Re$	Reynolds number
$t$	time, s
$T, T_l, T_s, T_a$	temperature, K
$T_0$	reference temperature for density definition, K
$T_f$	melting point of pure metal (Al), K
$T_{ref}$	reference temperature for enthalpy definition, K
$\Delta T$	undercooling, K
$\Delta T_N$	mean nucleation undercooling corresponding to maximum nucleation rate, K
$\Delta T_\sigma$	standard deviation of the Gaussian distribution, K
$\mathbf{u}_l, \mathbf{u}_s, \mathbf{u}_a$	velocity vector, $\text{m s}^{-1}$
$\mathbf{u}^*$	interface velocity, $\text{m s}^{-1}$
$U_{ls}(= -U_{sl}),$ $U_{la}(= -U_{al}),$ $U_{sa}(= -U_{as})$	momentum exchange rate, $\text{kg m}^{-2} \text{s}^{-2}$
$U_{ls}^d, U_{la}^d, U_s^d$	momentum exchange due to drag force, $\text{kg m}^{-2} \text{s}^{-2}$

\*Corresponding author, email t.wang@gi.rwth-aachen.de

$U_{ls}^p$	momentum exchange due to phase change, $kg\ m^{-2}\ s^{-2}$
$\beta_C$	solutal expansion coefficient
$\beta_T$	thermal expansion coefficient, $K^{-1}$
$\mu_l, \mu_s, \mu_a$	viscosity, $kg\ m^{-1}\ s^{-1}$
$v$	growth rate, $m\ s^{-1}$
$\rho_l, \rho_s, \rho_a$	density, $kg\ m^{-3}$
$\bar{\tau}_l, \bar{\tau}_s, \bar{\tau}_a$	stress-strain tensors, $kg\ m^{-1}\ s^{-2}$
subscripts $l, s, a$	denote liquid, solid and air phases respectively

**Introduction**

Melt convection and grain movement play an important role in the casting solidification process and greatly influence the formation of grain structures and solute segregation. In general, the melt convection and grain movement are a result of gravitational force. The densities within the melt are different due to the variation of temperature and concentration, and the density differences under the gravitational field cause convection in the melt, known as thermosolutal convection. Similarly, the density differences between the grains and the bulk melt cause grain movement, known as solid sedimentation or grain floating. An additional driving force for melt convection and grain movement is solidification shrinkage. It is well known that solidification shrinkage is the main reason for the formation of shrinkage cavities and one of the dominate reasons for porosity, hot/cold tearing, stress, deformation etc. Shrinkage force could somehow affect the flow pattern and the formation of macrosegregation, as described by Campbell.<sup>1</sup> For simplification, the vast majority of casting solidification models neglect the shrinkage induced flow (feeding flow). Thermosolutal convection modelling, without consideration of shrinkage effect, is generally carried out using the well known Boussinesq approximation.<sup>2</sup> This considers the density difference due to thermosolutal effects for momentum equations to model the thermosolutal convection, and a constant density for mass continuity equations to keep volume constant. The shrinkage effect has been ignored in the authors' previous work.<sup>3-6</sup>

To consider shrinkage flow further, the modelling of free surfaces is necessary because the shape of a free surface and the physical values near free surfaces dynamically change during solidification. A few publications have already dealt with the prediction of moving free surface formation. A good review is given by Ehlen.<sup>7</sup> An excellent algorithm is used by Mostaghimi *et al.*<sup>8</sup> Impact and solidification of a tin droplet on a steel plate is simulated and good agreement is found when the results are compared with experiments. Other publications model the sequential impact and solidification of two molten droplets on a solid surface or surface cooling by an impinging water drop. Commercial Software FLOW-3D models the solidifying free surface in its full Navier-Stokes model. Ehlen<sup>7</sup> has developed a new mathematical model and algorithm to simulate the solidification of moving free surfaces. It reformulates

the well known Volume of Fluid (VOF) method to be used with solidifying surface cells and temperature dependent liquid densities. This model has been applied to simulate the formation of deep shrinkage cavities in steel and Al-Si castings.

In this paper, the moving free surface caused by solidification shrinkage is tracked using a three phase volume averaging approach. In addition, the melt density is assumed to be temperature and concentration dependent, so that both the shrinkage flow and the thermosolutal convection can be taken into account. The moving free surface is defined as the interface between the melt and air. Particular attention is paid to the change of heat, momentum and pressure near the free surface. Meanwhile, the model considers the nucleation and growth of globular equiaxed grain growth, solute transport by diffusion and convection. Finally, the following points are discussed based on the calculations carried out by applying the present model to a benchmark casting:

- (i) the shape of free surface and the pressure change near the free surface with/without consideration of grain movement
- (ii) the flow pattern and macrosegregation formation with/without consideration of shrinkage flow.

**Model description**

There are three phases involved in the globular equiaxed solidification process, namely the liquid melt, the solidifying grains and the sucked air, denoted by  $l, s, a$  respectively. A volume averaging approach has been employed to formulate the conservation equations of mass, momentum, species and enthalpy for the three phases.

**Conservation Equations**

The conservation equations of mass, momentum, species, enthalpy and grain transport are shown as follows

Mass:

$$\frac{\partial}{\partial t} (f_l \rho_l) + \nabla \times (f_l \rho_l \mathbf{u}_l) = M_{sl} \dots \dots \dots (1)$$

$$\frac{\partial}{\partial t} (f_s \rho_s) + \nabla \times (f_s \rho_s \mathbf{u}_s) = M_{ls} \dots \dots \dots (2)$$

$$\frac{\partial}{\partial t} (f_a \rho_a) + \nabla \times (f_a \rho_a \mathbf{u}_a) = 0 \dots \dots \dots (3)$$

$$f_l + f_s + f_a = 1 \dots \dots \dots (4)$$

Momentum:

$$\frac{\partial}{\partial t} (f_l \rho_l \mathbf{u}_l) + \nabla \times (f_l \rho_l \mathbf{u}_l \otimes \mathbf{u}_l) = -f_l \nabla p + \nabla \times \bar{\tau}_l + f_l \rho_l \mathbf{g} + \mathbf{U}_{sl} + \mathbf{U}_{al} \dots \dots \dots (5)$$

$$\frac{\partial}{\partial t} (f_s \rho_s \mathbf{u}_s) + \nabla \times (f_s \rho_s \mathbf{u}_s \otimes \mathbf{u}_s) = -f_s \nabla p + \nabla \times \bar{\tau}_s + f_s \rho_s \mathbf{g} + \mathbf{U}_{ls} + \mathbf{U}_{as} \dots \dots \dots (6)$$

$$\frac{\partial}{\partial t} (f_a \rho_a \mathbf{u}_a) + \nabla \times (f_a \rho_a \mathbf{u}_a \otimes \mathbf{u}_a) = -f_a \nabla p + \nabla \times \bar{\tau}_a + f_a \rho_a \mathbf{g} + \mathbf{U}_{la} + \mathbf{U}_{sa} \dots \dots \dots (7)$$

where

$$\begin{aligned} \bar{\tau}_l &= \mu_l f_l \times [\nabla \otimes \mathbf{u}_l + (\nabla \otimes \mathbf{u}_l)^T] \\ \bar{\tau}_s &= \mu_s f_s \times [\nabla \otimes \mathbf{u}_s + (\nabla \otimes \mathbf{u}_s)^T] \\ \bar{\tau}_a &= \mu_a f_a \times (\nabla \otimes \mathbf{u}_a + (\nabla \otimes \mathbf{u}_a)^T) \end{aligned}$$

Species:

$$\frac{\partial}{\partial t} (f_l \rho_l c_l) + \nabla \times (f_l \rho_l \mathbf{u}_l c_l) = \nabla \times (f_l \rho_l D_l \nabla \times c_l) + C_{sl} \quad (8)$$

$$\begin{aligned} \frac{\partial}{\partial t} (f_s \rho_s c_s) + \nabla \cdot (f_s \rho_s \mathbf{u}_s c_s) \\ = \nabla \cdot (f_s \rho_s D_s \nabla \cdot c_s) + C_{ls} \end{aligned} \quad (9)$$

Enthalpy:

$$\begin{aligned} \frac{\partial}{\partial t} (f_l \rho_l h_l) + \nabla \cdot (f_l \rho_l \mathbf{u}_l h_l) \\ = \nabla \cdot (f_l k_l \nabla \cdot T_l) + Q_{sl} + Q_{al} \end{aligned} \quad (10)$$

$$\begin{aligned} \frac{\partial}{\partial t} (f_s \rho_s h_s) + \nabla \cdot (f_s \rho_s \mathbf{u}_s h_s) \\ = \nabla \cdot (f_s k_s \nabla \cdot T_s) + Q_{ls} + Q_{as} \end{aligned} \quad (11)$$

$$\begin{aligned} \frac{\partial}{\partial t} (f_a \rho_a h_a) + \nabla \cdot (f_a \rho_a \mathbf{u}_a h_a) \\ = \nabla \cdot (f_a k_a \nabla \cdot T_a) + Q_{la} + Q_{sa} \end{aligned} \quad (12)$$

where

$$\begin{aligned} h_l &= \int_{T_{ref}}^{T_l} c_{p(l)} dT + h_l^{ref} & h_s &= \int_{T_{ref}}^{T_s} c_{p(s)} dT + h_s^{ref} \\ h_a &= \int_{T_{ref}}^{T_a} c_{p(a)} dT + h_a^{ref} \end{aligned}$$

Grain Transport:

$$\frac{\partial}{\partial t} n + \nabla \times (\mathbf{u}_s \times n) = N \quad \dots \quad (13)$$

All symbols are defined in the list of symbols above.

Equations (1)–(12) are given by the FLUENT user manual.<sup>12</sup> Equation (13) is a user defined equation describing the grain nucleation and transportation. All of the conservation equations (1)–(13) are numerically solved by the CFD FLUENT software, Version 6.1. The corresponding source terms  $\mathbf{U}_{xx}$ ,  $M_{xx}$ ,  $Q_{xx}$ ,  $N$  are dependent on physical problems. Their definitions will be described below. Further details are given in Refs. (3)–(6). The main difference in the current work is that the presence of the air phase is modelled, i.e. the shrinkage flow effect is considered further. Note that the air has no mass transfer with other phases and therefore the source term of equation (3) is zero. The species calculation has been omitted for the air phase since there is no species mass fraction within the air phase.

**Nucleation, globular grain growth and mass transfer**

A three parameter heterogeneous nucleation law by Rappaz<sup>9</sup> has been employed to model grain nucleation. This approach is based on the assumption that many potential nucleation sites exist in the melt. The under-

cooling  $\Delta T$  serves as the driving force for nucleation. A Gaussian distribution is used to describe the statistical outcome of the nucleation sites as follows

$$\frac{dn}{d\Delta T} = \frac{n_{max}}{(2\pi)^{1/2} \times \Delta T_\sigma} \times \exp\left[-1/2\left(\frac{\Delta T - \Delta T_N}{\Delta T_\sigma}\right)^2\right] \quad (14)$$

The characteristics of this distribution (mean undercooling  $\Delta T_N$ , standard deviation  $\Delta T_\sigma$  and total density of grains  $n_{max}$ ) can be determined via exponential observations. In order to apply this nucleation law in the numerical model  $N$  in equation (13) is defined as

$$dn/dt = dn/d(\Delta T) \times d(\Delta T)/dt.$$

Solving equations (1)–(11) gives the average temperature of a volume element  $T$  and the average species mass fraction (concentration) in the liquid  $c_l$ . For globular solidification the grain growth is equivalent to the movement of the proceeding solid/liquid interface. For a Zener type diffusion field around a sphere,<sup>10</sup> the solute gradient at the interface is  $G_c^* = -2(c_l^* - c_l)/d_s$ . The solute balance at the interface is  $v \times (c_l^* - c_s^*) = -D_l \times G_c^*$ . Therefore, the globular grain growth rate  $v$  is given by

$$v = \frac{2D_l}{d_s} \frac{c_l^* - c_l}{c_l^*(1-k)} \quad \dots \quad (15)$$

The growth factor is defined as  $g_z = 2D_l/[d_s(1-k)]$  with the units  $m s^{-1}$ . Therefore equation (15) becomes

$$v = g_z(c_l^* - c_l)/c_l^* \quad \dots \quad (16)$$

where  $c_l^*$  is the liquid solute concentration at the solid/liquid interface. Based on the assumption of thermodynamic equilibrium at the interface,  $c_l^*$  can be calculated by  $(T/T_f)/m$ .  $T_f$  is the melting point of the solvent and  $m$  is the slope of the liquidus. During solidification, the solid/liquid interface areas of all grains within a volume element ( $n \times \pi d_s^2$ ) grow as the rate  $v$ . Because of the grain impingement, the total grain surface has to be corrected by an Avrami factor  $(1-f_s)$ . The mass transfer rate  $M_{ls}$  is thus

$$M_{ls} = -M_{sl} = v \times (n \times \pi d_s^2) \times \rho_s \times (1-f_s) \quad (17)$$

Grain size or diameter is related to the solid fraction and grain density within a control element, calculated by

$$d_s = \left(\frac{6f_s}{\pi \times n}\right)^{1/3} \quad \dots \quad (18)$$

**Momentum transfer**

Phase interactions (e.g. drag and friction) denoted by the superscript  $d$  and phase change denoted by superscript  $p$  are considered in order to calculate the momentum source terms. Therefore for a liquid/solid mixture

$$\mathbf{U}_{ls} = -\mathbf{U}_{sl} = \mathbf{U}_{ls}^p + \mathbf{U}_{ls}^d \quad \dots \quad (19)$$

with  $\mathbf{U}_{ls}^p = \mathbf{u}^* \times M_{ls}$  and  $\mathbf{U}_{ls}^d = K_{ls}(\mathbf{u}_l - \mathbf{u}_s)$ .  $\mathbf{u}^* = \mathbf{u}_l$  for solidification and  $\mathbf{u}^* = \mathbf{u}_s$  for remelting. The drag force coefficient  $K_{ls}$  is calculated by employing the model developed by Wang et al.<sup>11</sup>

Published by Maney Publishing (c) W. S. Maney & Son Limited

$$K_{ls} = \frac{4\beta^2 \mu_1}{d_s^2} f_1^2 \dots \dots \dots (20)$$

$$\beta = \left[ \frac{9}{2} (1-f_1) \frac{2 + \frac{4}{3} \eta^5}{2 - 3\eta + 3\eta^5 - 2\eta^6} \frac{1}{C_p(\phi_e)} \right]^{1/2}$$

with

$$\eta = (1-f_1)^{1/3}$$

$$C_p(\phi_e) = \phi_e^2 \quad 0.0 < f_1 < 0.7$$

$$C_p(\phi_e) = 1.26 \log_{10} \left( \frac{\phi_e}{0.163} \right) \quad 0.7 < f_1 < 1.0$$

$d_s$  is the grain diameter given by equation (18) and  $C_p(\phi_e)$  is a correction factor which accounts for the shape of the dendrite envelope. The above calculation of drag force coefficient is a universal method and can be adapted for globular, equiaxed and columnar growth.  $\phi_e$  can be simplified to 1 in the case of globular growth.

The momentum source terms due to phase changes between the air and the solid or the liquid are neglected. Therefore for liquid/air and solid/air mixtures, the source terms are calculated by

$$U_{la} = -U_{al} = U_{la}^d = K_{la}(\mathbf{u}_l - \mathbf{u}_a) \dots \dots \dots (21)$$

$$U_{sa} = -U_{as} = U_{sa}^d = K_{sa}(\mathbf{u}_s - \mathbf{u}_a) \dots \dots \dots (22)$$

Schiller and Naumann's model is used for calculating  $K_{la}$ <sup>11</sup>

$$K_{la} = 3\mu_1 f_1 f_a C_D R_e / (4d_a^2) \dots \dots \dots (23)$$

where  $d_a$  is the characteristic diameter of air which is used for calculating drag force only. A smaller air diameter represents a bigger drag force.  $C_D$  is a drag coefficient that is based on the relative Reynolds number  $R_e$

$$C_D = \begin{cases} 24(1 + 0.15R_e^{0.687})/R_e & R_e \leq 1000 \\ 0.44 & R_e > 1000 \end{cases} \dots \dots \dots (24)$$

with

$$R_e = \frac{\rho_1 |\mathbf{u}_a - \mathbf{u}_l| d_a}{\mu_1}$$

Symmetric modelling is used for calculating  $K_{sa}$ . This is similar to Schiller and Naumann's model, the difference being that the average grain diameter of air and solid  $(d_a + d_s)/2$ , the mixed viscosity  $\mu_a f_a + \mu_s f_s$  and the mixed density  $\rho_a f_a + \rho_s f_s$  are used in the calculation instead of using the properties of a single phase only.

**Enthalpy transfer**

The source terms of enthalpy transfer for the liquid/air and the solid/air mixtures are calculated by

$$Q_{la} = Q_{la}^d = H_{la} \times (T_l - T_a) \dots \dots \dots (25)$$

$$Q_{sa} = Q_{sa}^d = H_{sa} \times (T_s - T_a) \dots \dots \dots (26)$$

Note that the parts due to phase change are neglected. The heat exchange coefficient  $H_{la}$  is calculated by the Ranz and Marshall model<sup>11</sup>

$$H_{la} = 6k_1 f_1 f_s Nu_p / d_a^2 \dots \dots \dots (27)$$

$$H_{sa} = h_{sa} f_s f_a \dots \dots \dots (28)$$

where  $Nu_p$  is the Nusselt number and  $h_{sa}$  is an empirical heat transfer coefficient independent of mass fraction.

**Species transfer**

Only the solute partition due to phase change is considered for the source term  $C_{ls}(= -C_{sl})$  of the species conservation equations. Therefore

$$C_{ls} = -C_{sl} = C_{ls}^p \dots \dots \dots (29)$$

$C_{ls}^p = c^* \times M_{ls}$  with  $c^* = k \times c_l$  for solidification and  $c^* = c_s$  for remelting. In order to predict the macrosegregation, a mixture concentration is defined as

$$c_{mix} = (c_l \times \rho_l \times f_l + c_s \times \rho_s \times f_s) / (\rho_l \times f_l + \rho_s \times f_s) \dots \dots \dots (30)$$

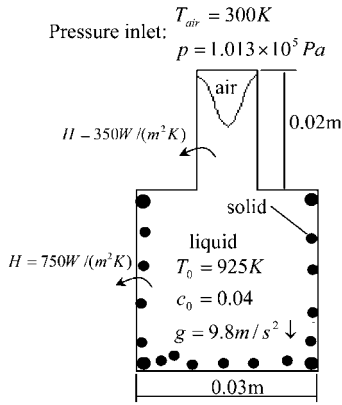
**Thermosolutal convection and shrinkage flow**

In general, shrinkages occur during solidification as a consequence of local density differences due to temperature inhomogeneity, concentration inhomogeneity and phase change. Density changes lead to local volume losses which are balanced by shrinkage flow. In contrast to thermosolutal convection which is driven by gravity only, the driving force for shrinkage flow is very high because it is driven by air pressure. In the current work, the reason for modelling shrinkage flow and thermosolutal convection is to apply the temperature and concentration dependent melt density to both the mass and momentum conservation equations. The top air following the feeding flow is sucked into the shrinking cavity. If the cooling by the mould is greater than the cooling of the top melt surface by radiation and air convection (e.g. in permanent mould casting), a free moving melt surface will be formed at the top during shrinkage. The free surface can be determined by the interface of air and melt in the three phase volume averaging model. The temperature and concentration dependent melt density is given by<sup>2</sup>

$$\rho_l = \rho_l(T, c_l) = \rho_0 [1 - \beta_T(T - T_0) - \beta_C(c_l - c_0)] \dots \dots \dots (31)$$

where  $\rho_0$  is a reference density for the liquid phase taken at temperature  $T_0$  and species mass fraction  $c_0$ , and  $\beta_T, \beta_C$  are the thermal and solutal expansion coefficients, respectively. The solid density  $\rho_s$  is assumed to be a constant, thus the shrinkage within the solid phase is neglected. The density defined by equation (31) accounts for the shrinkage flow when it appears in the mass conservation equation and the thermosolutal convection when it appears in the momentum conservation equations of the three phase model. The well known Boussinesq approximation considers equation (31) for the momentum equations only, to model the thermosolutal convection. Additional gravity terms (buoyancy force) are included in the momentum equations.<sup>2</sup>

Published by Maney Publishing (c) W. S. Maney & Son Limited



1 Benchmark ingot casting (Al-4Cu) and schematic diagram of three phases

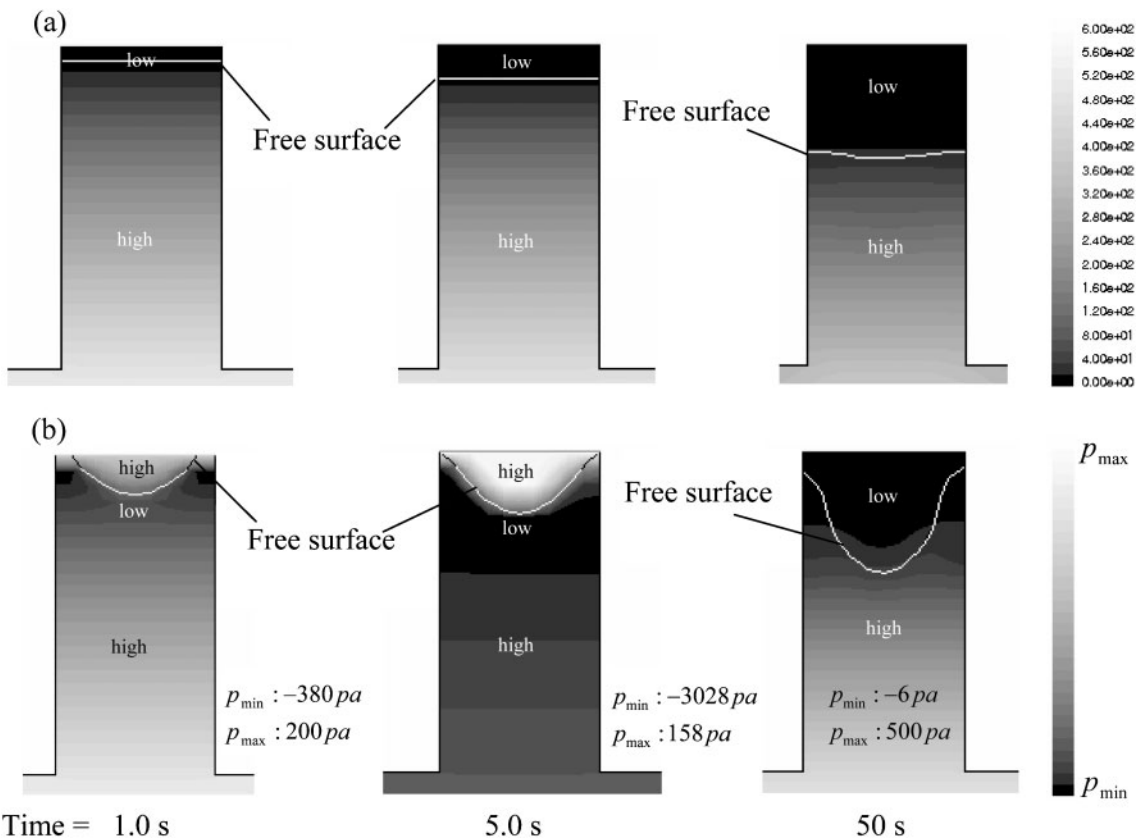
Results and Discussion

In order to study the free surface formation and the impact of shrinkage flow on the flow pattern and macrosegregation, a benchmark ingot casting was considered with the geometry shown in Fig. 1. The melt is supposed to be filled instantaneously. An inoculated Al-4Cu alloy was selected because of its almost globular equiaxed solidification morphology. Table 1 shows the physical properties of this alloy and of air.

Figure 2 shows the free surface and total pressure distribution near the free surface with and without grain movement. The free surface is defined as the isoline of air phase fraction = 50%. It is noted that both the shape of the free surface and the distribution

of total pressure look rather straight in the case of grain movement (Fig. 2a). The total pressure increases towards the bottom mainly due to the metallostatic pressure. A relatively low pressure occurs at the top area because the density of sucked air is small, causing a low hydrostatic pressure. Note that the standard 1 bar ambient pressure is excluded here since it occurs equally throughout the melt. The melt flow does not meet any hindering force while feeding the shrinking cavity since the grains near the free surface can move freely following the feeding melt. Although the packing limit of the solid fraction is set to 0.637, it is assumed that the cooling conditions make the heat transfer greater in the mould part and lower in the riser like part. This ensures that solidification occurs first in the mould part and then in the riser like part. It is only at the end of solidification (time = 50 s), that the solidification fraction finally reaches the packing limit; then the grain movement is constrained according to the packing limit assumption. Therefore, it can be seen that the shape of the free surface changes its curvature slightly because of the hindering of the constrainable grains.

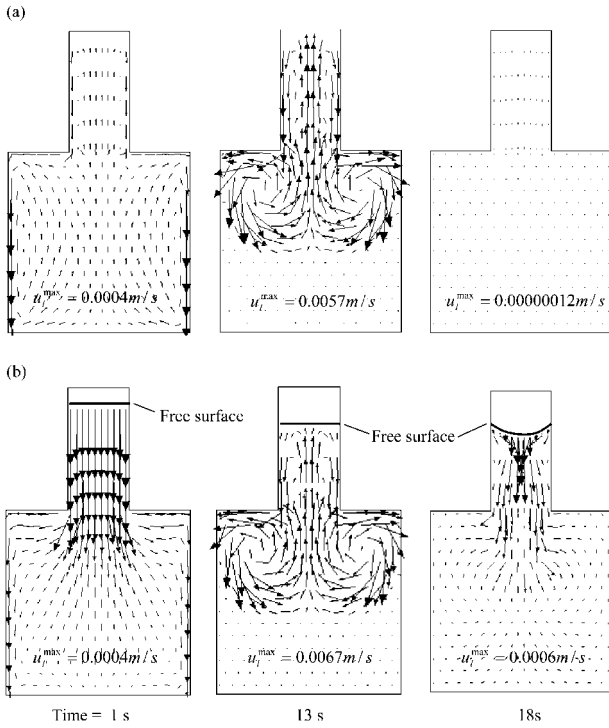
In the case of no grain movement (Fig. 2b), both the shape of the free surface and the distribution of total pressure are quite different compared with Fig. 2a. The shape of the free surface tends to be curved. The pressure above the free surface rises intensely. An area of negative pressure forms below the free surface. The melt is driven by the shrinkage force to feed the shrinking cavity, but is hindered by the no-move grains. A large pressure gradient is



a with grain movement; b without grain movement

2 Free surface (line) and total pressure distribution (grey scale) near free surface

Published by Maney Publishing (c) W. S. Maney & Son Limited



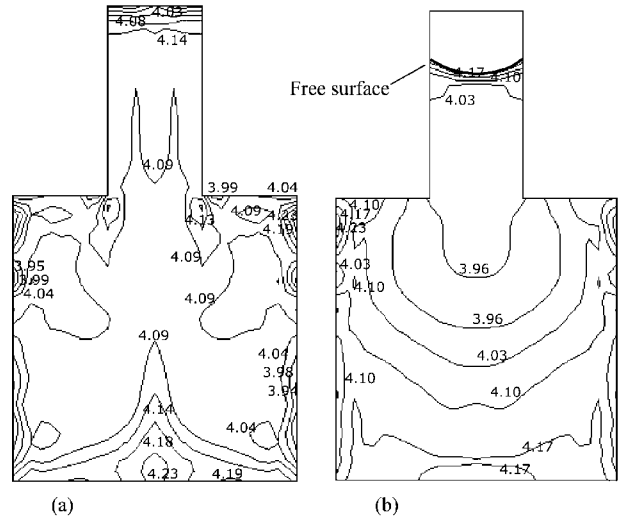
a without shrinkage flow (Boussinesq approach); b with shrinkage flow (three phase approach)

**3 Melt flow patterns consisting of thermosolutal convection and grain movement**

formed around the free surface due to the difference of forces. After the metallostatic pressure is also included, the distribution of total pressure finally looks like a high-low-high landscape (see Fig. 2b with time=1 and 5 s). At the end of solidification (time=50 s), the high pressure above the free surface disappears because the shrinkage induced pressure gradient has gone after the feeding flow path is closed.

**Table 1 Thermophysical and thermodynamic properties and nucleation parameter used in simulation<sup>6,11</sup>**

$\rho_l$	$\rho_l = \rho_0 [1 - \beta_T (T - T_0) - \beta(c_l - c_0)]$ $\rho_0 = 2606 \text{ kg m}^{-3}$ $\beta_T = 1 \times 10^{-4} \text{ K}^{-1}$ $\beta_c = -9.2 \times 10^{-3} (\text{wt}\%)^{-1}$
$\rho_{sr}, \rho_a$	2743, 1.225 $\text{kg m}^{-3}$
$k_l, k_s, k_a$	77, 153, 0.0242 $\text{W m}^{-1} \text{K}^{-1}$
$c_{p(l)}, c_{p(s)}, c_{p(a)}$	1179, 766, 1006.43 $\text{J Kg}^{-1} \text{K}^{-1}$
$D_l, D_s$	$5 \times 10^{-9}, 5 \times 10^{-13} \text{ m}^2 \text{ s}^{-1}$
$\mu_l, \mu_a$	$1.2 \times 10^{-3}, 1.8 \times 10^{-3}, 1.8 \times 10^{-5} \text{ kg m}^{-1} \text{ s}^{-1}$
$d_a$	$1.0 \cdot 10^{-5} \text{ m}$
$\mu_s = \begin{cases} \mu_l / f_s \left( (1 - f_s / f_s^c)^{-2.5 f_s^c} - (1 - f_s) \right) & \text{when } f_s < f_s^c \\ \infty & \text{otherwise} \end{cases}$	
with the packing limit $f_s^c = 0.637$	
$T_f$	933.5 K
$k$	0.145
$M$	-344 K
$\beta_T$	$1.2519 \cdot 10^{-3} \text{ K}^{-1}$
$\beta_C$	$-1.4388 \cdot 10^{-2}$
$n_{\text{max}}$	$2.5^{11} \text{ m}^{-3}$
$\Delta T_N$	20 K
$\Delta T_\sigma$	8 K



a without shrinkage flow; b with shrinkage flow

**4 Macrosegregation maps near solidification end, considering thermosolutal convection and grain movement ( $c_{\text{mix}} = 4.1\text{--}4.3 \text{ wt}\%$ )**

In fact, the cases represented by Fig. 2 are the extremes. The reality of grain movement is neither a completely free one nor a constraining one. Therefore the actual shape of the free surface and the distribution of total pressure should lie between Fig. 2a and b.

Figure 3 shows the flow pattern variation of a solidifying sample in the absence (Fig. 3a) and presence (Fig. 3b) of shrinkage flow. At the very beginning (time=1 s), it is noted that there are strong flows near the mould walls for both Fig. 3a and b. This is due to a fast melt cooling near the mould walls, increasing the density there and activating thermal convection. The solutal convection is minor because the solute has not yet piled up. In particular, the shrinkage flow from the top to feed the shrinking melt can be clearly seen in Fig. 3b. The shrinkage flow and thermal convection dominate the flow pattern at the beginning. As solidification proceeds, the flow becomes a combination of thermosolutal convection and shrinkage flow. Because of the solute partition and transport and the further melt cooling and heat transfer, the thermosolutal convection dominates the flow pattern and the shrinkage flow is hardly noticeable, although it does exist (see Fig. 3a and b with time=13 s). The velocity is low at the top of the riser like part in Fig. 3b as a result of the presence of sucked air. With further solidification, the space available for melt convection decreases and therefore thermosolutal convection becomes weaker (see Fig. 3a with time=18 s). However, the shrinkage flow is still active because of the assumption that the cooling condition ensures that the feeding path remains unblocked until the end of solidification (see Fig. 3b with time=18 s). It can be concluded that the shrinkage flow dominates the flow pattern in this situation.

Figure 4 shows the positive macrosegregation maps near the solidification end in the absence and presence of shrinkage flow. The absolute values of segregation in the cases shown in Fig. 4 are not big ( $c_{\text{mix}} = 3.94\text{--}4.23 \text{ wt}\%$ , compared with the initial

Published by Maney Publishing (c) W. S. Maney & Son Limited

concentration 4 wt-%) because the benchmark used for the simulation is small giving just a short solidification time. However, big differences can still be noticed when comparing the predicted segregation maps with and without consideration of the shrinkage flow. The obvious differences are:

- (i) at the bottom and centre of the ingot, the isoconcentration lines are convex in Fig. 4a and concave in Fig. 4b
- (ii) at the corners between the riser like part and the casting part, positive segregation is found in Fig. 4a and negative segregation in Fig. 4b
- (iii) since the volume shrinkage is considered, a clear free surface with a slight curve can be found in Fig. 4b.

Both Fig. 4a and b consider the thermosolutal convection and grain movement. The only difference of modelling is that shrinkage flow exists in Fig. 4b but not in Fig. 4a. Therefore it is shrinkage flow that causes the differences between the two parts.

According to the flow patterns shown in Fig. 3, it is known that grain movement leads to a solid sedimentation along the wall towards the bottom of the ingot and thermosolutal convection leads to an inner flow from the two sides to the centre. As a result, in Fig. 4a a narrow negative segregation zone is found at the sidewall bottom and a tower shape solute buildup is found at the centre bottom. In Fig. 4b, the shrinkage flow is considered. The shrinkage flow carrying the top melt brushes the solute away from the centre towards the two sides, causing bowl shaped isoconcentration lines.

The current work is focused on the modelling of globular equiaxed solidification, considering thermosolutal convection, grain movement and shrinkage flow on a macro scale. The solidified grains can be simplified as spheres. The three phase volume averaging model is actually not recommended for the simulation of the solidification process with complicated grain morphology (e.g. the solidification of higher concentration Al-Cu alloy). It is possible to simulate the dendritic growth of equiaxed and columnar grains using certain assumptions and modifications to the presented model. However this introduces significant complexities to the three phase volume averaging model, making the model more expensive.

In the three phase volume averaging model, a set of conservation equations of mass, momentum, enthalpy and species are solved for each phase. The phase transfers and interactions are very much dependent on the determination of source terms and exchange terms for the conservation equations. Therefore, special care should be taken in the determination of source/exchange terms with clear consideration of the physics. Despite these limitations, modelling of globular equiaxed solidification has broad prospects for engineering application. Many high performance materials require fine globular grains, e.g. the newly developed thixoforming process requires the prematerial to be made with spherical grains.<sup>6</sup> The authors have applied the presented model to the simulation of the rehotcasting process,<sup>13</sup> and have recently studied the motion of inclusions during continuous casting. The most

important phenomena which lead to the formation of shrinkage defects are:<sup>7</sup>

- (i) movement of the solidifying free surface (external shrinkage cavities)
- (ii) interruption of feeding flow (internal shrinkage cavities, shrinkage porosities)
- (iii) precipitation of gas bubbles (hydrogen porosities)
- (iv) different shrinkage velocities of the unstable solid network in the mushy zone (hot tearing)
- (v) obstruction of solid shrinkage by the mould (hot tearing).

The current model can effectively predict the phenomena described in item (i). If solidification leads to a situation where a liquid reservoir is completely surrounded by solid and thus cuts off all feeding possibilities, internal shrinkage cavities or shrinkage porosities form (item (ii) above). At present, this problem cannot be modelled. However a potential idea will be tried. In case the local pressure reaches the critical pressure for pore nucleation due to the pressure drop within a closing zone, a suitable amount of air (alloy vapour) will be artificially generated to occupy the pores thus keeping the volume constant. Hydrogen porosities together with internal shrinkage porosities are analysed as the consequences of comprehensive interactions<sup>14</sup> between pressure decrease due to shrinkage flow, oxide entrapment and hydrogen diffusion/solubility. These call for a very complicated model, not included in the current work. The shrinkage flow has significant effects on the formation of hydrogen porosities. However, hydrogen porosities might have slight effects on the shrinkage flow thus for grain movement. In this work, the density of solid phase is kept constant. Therefore items (iv) and (v) have not been considered, i.e. the hot tearing due to internal stresses and obstruction by the mould are neglected.

## Conclusions

The developed three phase volume averaging model is applied to simulate a benchmark ingot casting. The results show that the presented model is feasible to model the thermosolutal convection together with grain movement and shrinkage flow for globular equiaxed solidification. The following remarks could be concluded from the tested calculation.

1. The shape of the free surface and the distribution of total pressure near the free surface are almost straight in the case of free grain movement, and largely curved in the case of no grain movement. It was found that the pressure rises intensely above the free surface in the case of no grain movement.

2. For the benchmark casting, comprehensive flow patterns are first dominated by thermal convection and shrinkage flow, then by thermosolutal convection and finally by shrinkage flow during solidification.

3. Absolute macrosegregation is not serious, but a significant difference in segregation patterns is found when comparing cases with and without considering the shrinkage flow. The isoconcentration lines are convex in the absence of shrinkage flow and concave in the presence of shrinkage flow.

## Acknowledgements

Financial support for this research has been provided by the German Science Foundation (DFG) as part of the collaborative research centre SFB 370.

## References

1. J. CAMPBELL: 'Castings'; 1991, Oxford, Butterworth-Heinemann
2. T. U. KAEMPFER and M. RAPPAZ: Proc. 9th Conf. on 'Modelling of casting, welding and advanced solidification processes', Aachen, Germany, August 2000, TMS, 640–645.
3. M. WU and A. LUDWIG: *Adv. Eng. Mater.*, 2003, **5**, 62–66.
4. M. WU, A. LUDWIG, A. BÜHRIG-POLACZEK, M. FEHLBIER and P. R. SAHM: *Int. J. Heat Mass Transfer*, 2003, **46**, 2819–2832.
5. A. LUDWIG, M. WU, T. WANG and A. BÜHRIG-POLACZEK: Proc. 3rd Conf. on 'Computational modelling and simulation of materials', Sicily, Italy, March 2004, TMS, (to be published).
6. A. LUDWIG and M. WU: *Metall. Mater. Trans.*, 2002, **33A**, 3673–3683.
7. G. EHLEN: 'Transient numerical simulation of complex convection effects during solidification in casting and welding', PhD Thesis, Aachen, Germany, Shaker-Verlag, 2004.
8. M. BUSSMANN, MOSTAGHIMI and S. CHANDKA: 'On a three-dimensional volume tracking model of droplet impact', *Physics of Fluids*, 1999, **11**, 1406–1417.
9. M. RAPPAZ and C.-A. GANDIN: *Acta Metall. Mater.*, 1993, **41**, 345–360.
10. W. KURZ and D. J. FISHER: 'Fundamentals of solidification'; 1985, Lausanne, Trans Tech Publications Ltd.
11. C. Y. WANG, S. AHUJA, C. BECKERMANN and H. C. DE GROH III: *Metall. Mater. Trans. B*, 1995, **26B**, 111–119.
12. 'FLUENT 6.1 User's Guide'; 2003, Lebanon, NH, USA, Fluent Inc.
13. T. WANG, B. PUSTAL and M. ABONDANO *et al.*: *Tran. Nonferrous Met. China*, 2004, (to be published).
14. I. OHNAKA, A. SUGIYAMA and H. OPDA *et al.*: Proc. 6th Conf. on 'Modelling of casting and solidification processes', Kaohsiung, August 2004, Hwang Weng-Sing, 3–11.